lubricants

MDPI

Article

Effect of Pressure on the Microstructure and Wear Performance of Cr-Mn-Mo Alloyed Steel Prepared by Squeeze Casting

Yuan Zhuang [1,*], Yujiang Hao [1], Lei Guo [2] and Xinhao Wu [3]

[1] School of Engineering, University of Aberdeen, Aberdeen AB24 3FX, UK
[2] College of Mechanical and Electrical Engineering, Northeast Forestry University, Harbin 150040, China
[3] Adam Smith Business School, University of Glasgow, Glasgow G12 8QQ, UK
* Correspondence: 18253978522@163.com

Abstract: In this study, the effects of applied pressure (0, 90, 120, and 150 MPa) during solidification on the microstructure, mechanical properties, and impact–abrasive wear resistance of Cr-Mn-Mo steel prepared by squeeze casting were systematically investigated. The results demonstrated that the materials produced under pressure showed smaller grains compared to those of the samples fabricated without pressure. Compared to the unpressurized sample, the grain diameter of the sample prepared at 120 MPa decreased by 37.7%, the length of the primary arm shortened by 40.7%, and the spacing of the secondary arm contracted by 14.1%. Furthermore, the impact toughness results indicated that the samples prepared without pressure exhibited brittle fracture characteristics, whereas quasi-destructive fractures predominated in the samples prepared at 120 MPa. Simultaneously, three-point bending strength exhibited a gradual increase with increasing pressure, reaching a maximum value of 855.5 MPa when prepared under 150 MPa. Additionally, the impact–abrasive wear resistance of Cr-Mn-Mo alloyed steel produced by squeeze casting was significantly enhanced compared to the samples produced without pressure. The samples without external pressure exhibited a combination of abrasive and adhesive wear, whereas the wear characteristics of the samples prepared under pressure includes grooves, cutting marks, flaking pits, and accumulating ridges.

Keywords: squeeze casting; Cr-Mn-Mo alloyed steel; impact–abrasive wear; wear mechanism

Citation: Zhuang, Y.; Hao, Y.; Guo, L.; Wu, X. Effect of Pressure on the Microstructure and Wear Performance of Cr-Mn-Mo Alloyed Steel Prepared by Squeeze Casting. *Lubricants* **2024**, *12*, 392. https://doi.org/10.3390/lubricants12110392

Received: 26 September 2024
Revised: 2 November 2024
Accepted: 12 November 2024
Published: 14 November 2024

1. Introduction

Wear is one of the most common industrial problems that causes material wastage and the degradation of mechanical performance, resulting in significant economic losses [1–3]. Under the operational circumstances for many wear-resistant materials, the service rate experiences tend to be greater in medium- to low-stress environments compared to that in high-stress situations [4]. Low–medium alloyed wear-resistant steels have long been favored in conditions of low or moderate impact wear due to their ability to maintain a good match of strength and toughness with a lower preparation cost [5]. Among the various low–medium alloyed steels, the Cr-Mn-Mo alloyed steel is a typical one, which is frequently utilized as essential components for wear resistance, including ball milling liners, plates for jaw crushers, hammer heads, and so on. When used as a mill liner, it is often fabricated by sand casting or evaporative pattern casting [6,7]. However, these methods are primarily reliant on gravitational replenishment, which significantly limits their effectiveness. As a result, they are prone to causing numerous defects, including porosity, trachoma, shrinkage, loosening, grain coarseness, and pronounced segregation [8–10]. Such deficiencies severely restrict the potential performance of the material, rendering the liner suboptimal in terms of wear resistance. Therefore, it is essential to improve the casting process to address these issues.

Squeeze casting is a metal-forming process that facilitates the solidification of molten metal under high pressure within the mold. It provides numerous benefits, such as increased productivity, fewer casting defects, improved product performance, and decreased

manufacturing costs [11–13]. Furthermore, this method is classified as a green casting technology characterized by low energy consumption and the absence of sand and risers, thereby eliminating the pollution associated with waste sand, which aligns with the objectives of sustainable development. In comparison to die casting, the yield strength of workpieces produced through squeeze casting increases by 10% to 15%, whereas elongation and fatigue strength may achieve enhancements of 50% to 80% [14]. Additionally, many research studies have demonstrated that this approach can significantly improve the toughness and strength of nonferrous metals as well as their composites [15,16]. Tirth [17] studied the effect of pressure on the microstructures, porosity, and hardness of cast aluminum 2124, 2218, and 6063 alloys. The materials were developed at seven pressure variations from 0 to 150 MPa, and the results illustrated that the pressure of 100 MPa gives a better increment in mechanical properties, and the solubility and freezing coefficients depend on the pressure in addition to the composition and temperature. Nasker [18] investigated the influences of SiC nanoparticle content on the microstructural modification and mechanical properties of a squeeze cast Mg-5.0Al-2.0Ca-0.3Mn alloy, and the results showed that the samples all exhibited a higher strain hardening exponent and rate compared to the samples prepared without pressure. However, ferrous wear-resistant metals present challenges for squeeze casting due to their high melting point and limited fluidity, leading to sluggish progress in the research and application of squeeze casting for these materials. Currently, the effect of squeeze pressure on the microstructure and wear resistance of ferrous metals has received limited attention. Particularly, the characteristics of impact–abrasive wear resistance in squeeze casting Cr-Mn-Mo alloy steel and its variation with pressure remains unexplored.

In the current study, we prepared Cr-Mn-Mo alloy steel liners under various squeeze pressures (0 MPa, 90 MPa, 120 MPa, and 150 MPa) to examine the effect of pressure on the microstructure, mechanical characteristics, and wear resistance of the tested materials. Techniques such as optical microscopy (OM), scanning electron microscopy (SEM), and X-ray diffraction (XRD) were employed to analyze the microstructure, elemental content and morphology, along with the physical phases, of the materials. The mechanical properties of the tested steels were assessed by conducting tests on hardness, impact toughness, and three-point bending strength to explore the effect of pressure. Furthermore, an impact–abrasive wear testing device was utilized to assess the wear property of the prepared materials, including the quantitative influence of pressure and wear mechanisms. Meanwhile, a schematic of the wear mechanisms was proposed.

2. Materials and Methods

2.1. Materials

The raw materials utilized in the current study consist of scrap steel, ferrochrome, ferromolybdenum, ferromanganese, and several other alloying materials. An induction furnace operating at medium frequency was utilized for melting the alloy materials, employing the alkaline magnesium sand crucible as the container, and melting the raw materials under an atmospheric environment. Initially, scrap steel was added until fully melted; subsequent additions included ferrochrome, ferromolybdenum, ferromanganese, copper, and additional alloying materials to modify the composition of the liquid steel. Before completion, ferrosilicon was introduced into the furnace for pre-deoxidation. Upon completion, aluminum wire and rare-earth ferrosilicon were added to the casting ladle for final deoxidation and treatment. A direct-reading spectrometer was employed to examine the steel's composition, with the chemical makeup of the steel detailed in Table 1.

Table 1. Chemical makeup of the Cr-Mn-Mo alloyed steel (wt.%).

Element	C	Cr	Mn	Mo	Cu	Si	P	S
Content	0.61	4.02	0.52	0.57	0.5	0.04	0.05	0.04

2.2. Fabrication of the Cr-Mn-Mo Alloyed Steel

The schematic diagram for the preparation of the liner via the squeeze casting technique is shown in Figure 1. The direct liquid forging method is adopted on a vertical THP-1600T liquid forging machine, and the procedures for the experiment are detailed as follows: (a) Melting of the raw materials: The alloy materials were melted in a medium frequency furnace to 1560–1600 °C, then the liquid metal was poured into the mold cavity, which was preheated to 200 °C. To prevent splashing of the liquid metal during pouring, a buffer pouring chamber was established at the center of the mold cavity, utilizing a profiling pressure head as the bottom. In consideration of the ease of connection between the profiling pressure head and the piston rod, the head was designed as a circular shape, and the depth of the pouring chamber measured 100–150 mm. The liquid metal was introduced into the buffer chamber until its level reached 5 mm below the parting surface. (b) Pressure applied: Given the placement of the liner working surface (liner crest) within the lower mold, the lower hydraulic cylinder was adopted to exert pressure, and the specific pressures applied during squeeze casting were set as 90 MPa, 120 MPa, and 150 MPa. Considering the large thickness of the liner and the propensity for defects in the central region, the upper mold was segmented into two parts: a boost pressure head in the central section, which aligns with the location of the liner's wall thickness, and the external clamping portion of the upper mold. This design allows for effective compensation and shrinkage of the thicker areas. (c) Pressure maintenance and solidification processes: The applied pressure should be maintained for a certain time to facilitate both the solidification and proper feeding of the material. Furthermore, the duration for maintaining pressure can be determined through the square root law of metal solidification time: $T = (D/K)^2$, where D and K represent the equivalent thickness at the final solidification position and solidification coefficient, respectively. (d) Pressure release and component extraction processes: Following the release of pressure, the mold was opened, and the parts were extracted. The connecting rod of the lower pressure head was fitted with a stripper plate, which comes into contact with the eject rod when the lower head is correctly positioned. Consequently, after the mold was opened, the lower head continued to ascend, thereby driving the eject rod to push the parts from the lower mold.

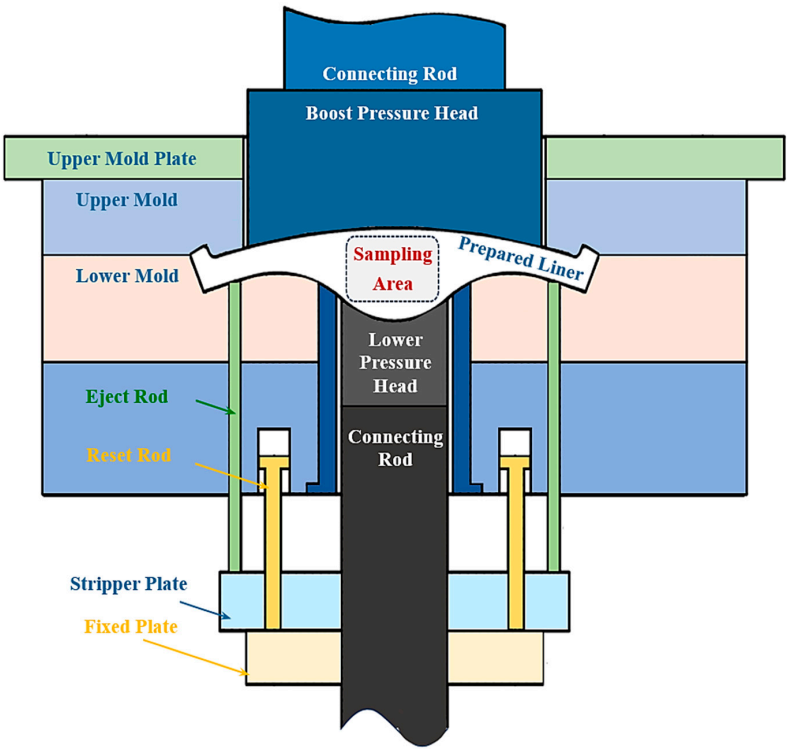

Figure 1. Schematic diagram for the preparation of the liner by squeeze casting.

2.3. Characterization of Microstructure and Mechanical Properties

Metallographic, hardness, impact, three-point bending strength, and wear samples were processed from the central region of the liner parts (Figure 1). The metallographic samples (10 mm × 10 mm × 10 mm) for microstructure observation were prepared. After grinding, polishing, and etching with 4% Nital solution, the microstructure of samples was investigated using a DM5000 optical microscope (OM) and EVO18 scanning electron microscope (SEM) equipped with EDS. Five typical fields of view were selected for each sample to be observed, photographed, and quantitatively analyzed. A quantitative metallographic examination was conducted, with the subsequent importation of the images into the Image Pro Plus program for acquisition, analysis, and quantitative calculations. The process included image acquisition, grayscale analysis, preprocessing, binarization processing, manual editing of images, and image determination. Metallographic determination encompassed grain size, aspect ratio (R), average length of primary dendrite arms (L_D), and average size of secondary dendrite arm spacing (SDAS), measured by the truncation method, as illustrated in Figure 2.

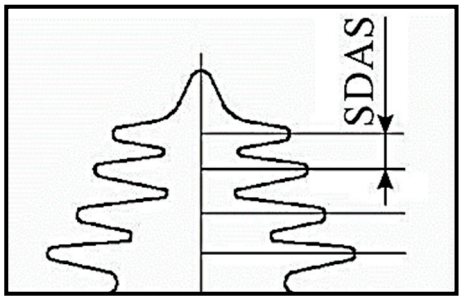

Figure 2. Measurement of SDAS size by the cutting line method.

According to the statistical restoration method, which resolves the three-dimensional information of the alloy microstructure through its low-dimensional data, thereby providing a validated approach to quantitatively calculate the phase volume fraction, this approach interprets the information of each phase and structure within the material's microstructure as an image composed of points, lines, surfaces, and bodies. The following relationship equation is established between these variables:

$$V_V = A_A = L_L = P_P$$

where V_V represents the volume fraction of the measured phase; A_A denotes the area occupied by the measured phase per unit of measurement area; L_L signifies the length of the measured phase per unit of measurement line; and P_P indicates the ratio of the total number of points measured to the number of points that fall within the measured phase.

By measuring the eutectic tissue area fraction and porosity area fraction from the two-dimensional metallographic dataset, three-dimensional information, including the eutectic tissue volume fraction (V_E) and porosity (V_P), can be derived. The measured individual data were processed according to the lower average method [19]:

$$M = \frac{1}{m}\sum_{j=1}^{m}\left(\frac{1}{n}\sum_{i=1}^{n}M_i\right)_j$$

where M represents the maximum values of length, area, and volume fraction; M_i denotes the actual measured values of length, area, and volume fraction; N signifies the number of measurements within a single metallographic image; m represents the number of observed areas; and i and j denote specific data points.

Furthermore, the phase analysis of the samples was carried out utilizing an XRD system (Ultima IV) with specific operational parameters: Cu Kα radiation at a wavelength of 1.54056 Å, a voltage of 36 kV, a current of 20 mA, a scanning angle span from 20° to 80°, a

scanning speed of 2 °/min, and a step size of 0.02°. The results were analyzed utilizing Jade 5. The hardness of the samples with a size of 10 mm × 10 mm × 10 mm was assessed using an HR-150C Rockwell hardness testing machine (Hengyi, Beijing, China). For each sample, five data points were recorded, and the average was calculated to obtain the final result. The impact toughness of the samples with a size of 10 mm × 10 mm × 55 mm was measured using a Charpy pendulum impact test conducted on a JB-50 experimental machine (Shidai, Beijing, China). Given the high hardness and low toughness of ZG60Cr4MnMoCu, the sample was not notched. Three samples were prepared under identical experimental conditions, and the test results were averaged. The fracture surface was analyzed using SEM to elucidate the destruction mechanism of the samples. A three-point bending strength test was conducted considering ZG60Cr4MnMoCu is classified as a low-plasticity material. The tests were performed on a WDW-1 electronic universal testing machine (Xinbiao, Jinan, China). Similarly, three samples (5 mm × 5 mm × 35 mm) were prepared under identical conditions, and the test results were averaged.

2.4. Impact–Abrasion Wear Test

As previously noted, low–medium alloyed steels are suitable for a wide range of industrial applications, and such applications necessitate resistance to the effects of impact and abrasive wear, which can be effectively simulated using an impact–abrasion wear test. Consequently, the impact wear test was conducted on an MLD-10 dynamic load abrasive wear tester (Chengxin Testing Equipment Co., Ltd., Zhangjiakou, China) to investigate the wear performance of the prepared steels. Figure 3 illustrates the schematic diagram of the impact–abrasive wear tests, where the wear process was conducted through the continuous rotation of the lower sample (counterpart ring with a size of 50 mm × 30 mm × 20 mm) and the perpendicular reciprocated motion of the upper sample (10 mm × 10 mm × 30 mm, experimental materials). The ring was fabricated from GCr12 steel. During the wear process, the upper sample was mounted on a holder connected to the impact hammer, operating at a frequency of 150 times/min, while the counterpart ring rotated at a speed of 200 r/min. Quartz sand with a size of a 10–20 mesh and a hardness of 800–1200 HV was selected as the abrasive. In addition, under the actual working conditions of ball mill liners (take Φ2.5 m type liner as an example), the impact toughness (impact energy per unit area) can be calculated as follows [20]:

$$E = \frac{mgh}{S} = \frac{7.05 \times 10 \times 2.5 \times \frac{2}{3}}{96.7 \times 41} = 0.0296\ \mathrm{J/m^2}$$

where m represents the mass of the grinding ball, which can be determined according to the density and diameter of the grinding ball; h denotes the free-fall height of the grinding ball, which can be regarded as two-thirds of the height of the ball mill; and S signifies the area of the liner. In the current study, the impact energy was configured to be 3 J, equating to a free-fall height of 30 mm for the impact hammer.

The wear samples underwent ultrasonic cleaning, followed by drying, and were subsequently weighed by a high-precision electronic balance (0.1 mg) to assess mass variation. Prior to the formal wear experiment, each sample underwent a pre-wear process lasting 30 min to grind the surface into a face contact condition. After that, the wear process was conducted for 120 min, with mass variation being recorded every 10 min. The tests were conducted three times under varying test conditions with new samples, and the average of the three measurements was considered the final result. After the wear test, the worn surfaces were examined by SEM to investigate the wear features and mechanism of the prepared materials.

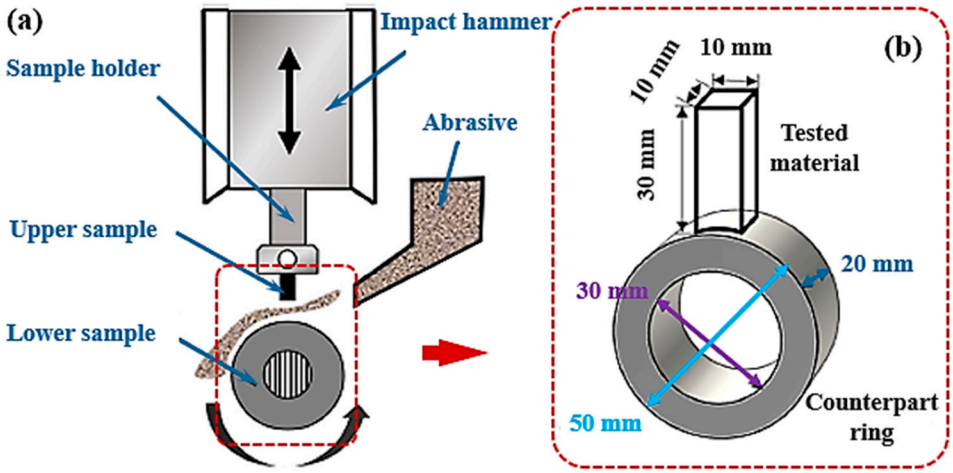

Figure 3. (**a**) Schematic diagram of the impact–abrasive wear tests; (**b**) Size of wear sample and counterpart ring.

3. Results and Discussion

3.1. Microstructure

Figure 4a–d illustrates the microstructure of the four tested samples at lower magnification, respectively. It can be seen that the four steels prepared with or without pressure all exhibit a dendritic structure, and the size of the dendrites varies significantly among different samples. The one without pressure shows thick and long primary dendrites, while those with pressure, however, have significantly smaller grains. Image Pro Plus 6.0 metallographic measurement software was utilized to conduct a statistical analysis of the microstructural parameters, including primary dendrite arm length (LD), average grain size (D), average grain aspect ratio (R), and average secondary dendrite arm spacing (SDAS). The results are presented in Table 2, with an error range of the measurement results being within 1%. The grain of the samples under pressure was observed to be finer and denser than that of the sample without pressure. The data presented in the table indicate that the grain size decreases sequentially with increasing prepared pressure. Compared with the unpressurized sample, the grain diameter of the sample prepared at 120 MPa decreased by 37.7%, the length of the primary arm shortened by 40.7%, and the spacing of the secondary arm contracted by 14.1%. Moreover, there was minimal difference between the sizes of the samples prepared at 120 MPa and 150 MPa. In addition, the length-to-diameter ratio reached a maximum at 120 MPa, and the spacing of the secondary dendrite arms progressively increased. These findings suggest that the squeeze casting process significantly influences grain refinement, which is in agreement with the previous findings of Qiu [21] and Huang [22].

The microstructures of the samples prepared under pressure at higher magnification are shown in Figure 4b′–d′, where they consist of martensite, bainite, residual austenite, and carbides. This occurs due to the addition of chromium (Cr), manganese (Mn), molybdenum (Mo), and other elements to enhance hardenability, resulting in the formation of martensite in the air-cooled state. Furthermore, chromium and molybdenum facilitate the separation of the pearlitic and austenitic zones, allowing for the formation of a certain amount of bainite. As illustrated in the figure, the martensite slats of the samples under pressure are significantly finer, with very fine white carbides distributed at the grain boundaries and edges of the martensite slats. These carbides exhibit nanometer-scale sizes and are present in particulate form. An analysis of the carbides in the sample prepared at 90 MPa using an X-ray diffractometer (XRD), as shown in Figure 5a, indicated that these carbides include the types M_3C, M_7C_3, and $M_{23}C_6$. According to the Fe-C-Cr phase diagram, when the chromium content exceeds 1%, M_3C and M_7C_3 carbides will form. In contrast, $M_{23}C_6$ carbides may originate from the enrichment of alloying elements due to the polarization of

Cr, Mn, and C elements between dendrites. In addition, it is evident that with an increase in pressure, the martensite plate size of each sample decreases correspondingly; moreover, the average width of the martensite for each sample was measured using Image Pro Plus. The results, depicted in Figure 5b, indicate that the martensite size is inversely proportional to pressure.

Table 2. Analysis results of samples prepared under different pressures.

Pressure (MPa)	D (μm)	L_D (μm)	R	SDAS (μm)
0	23.96 ± 1.29	130.64 ± 1.64	2.05 ± 0.33	27.02 ± 2.10
90	18.49 ± 1.23	139.82 ± 1.58	2.99 ± 0.24	22.15 ± 1.19
120	14.88 ± 1.17	77.46 ± 1.44	2.43 ± 0.27	23.18 ± 1.67
150	14.79 ± 0.96	224.24 ± 1.27	2.50 ± 0.19	27.56 ± 1.63

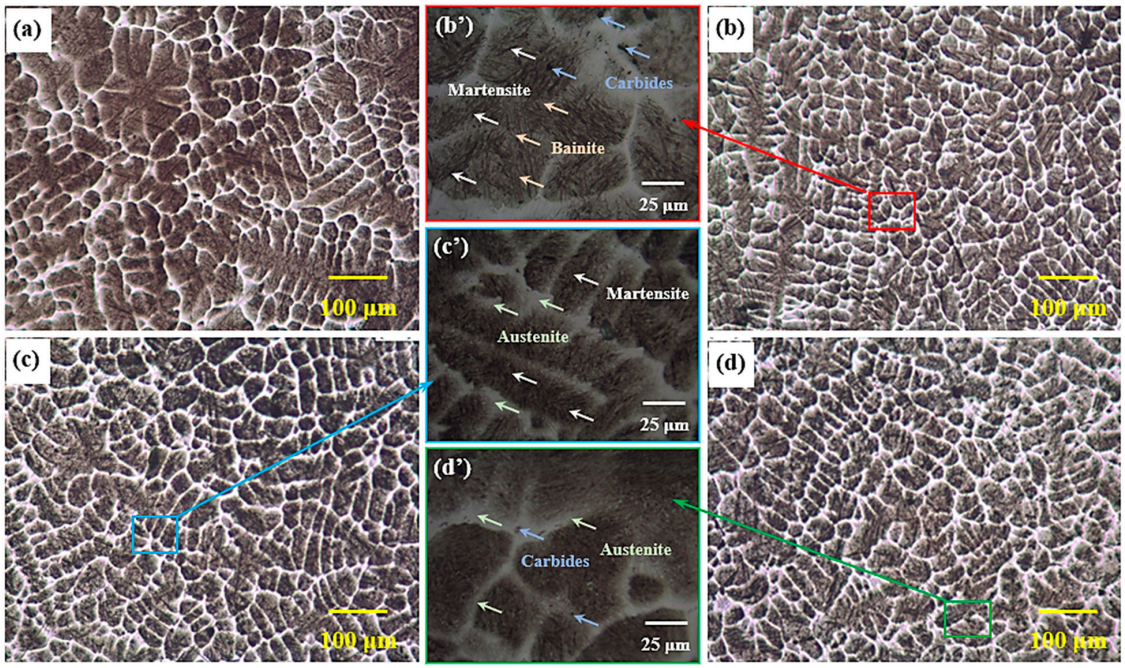

Figure 4. (**a**–**d**) Microstructure of the samples prepared under 0 MPa, 90 MPa, 120 MPa, and 150 MPa at lower magnification; (**b′**–**d′**) Microstructure of the samples prepared under 90 MPa, 120 MPa, and 150 MPa at higher magnification.

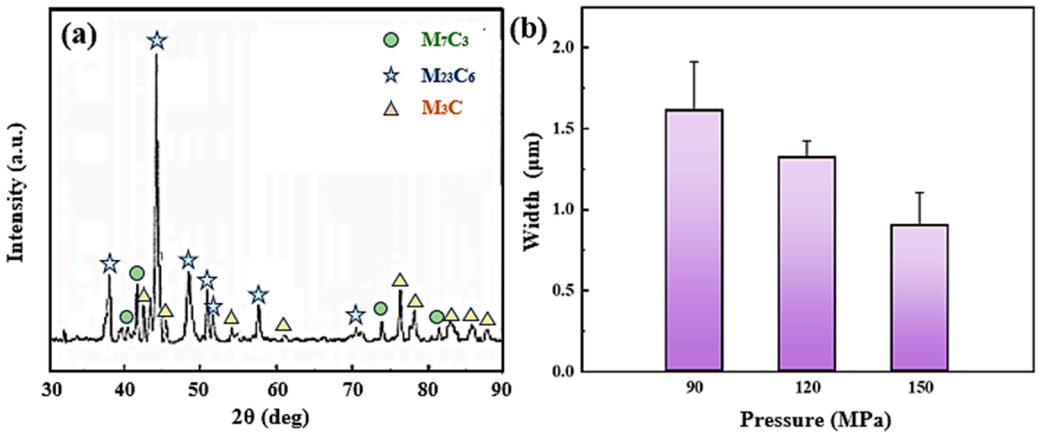

Figure 5. (**a**) XRD analysis results of the sample prepared at 90 MPa; (**b**) Comparison of the martensite diameter of samples prepared at various pressures.

3.2. Mechanical Properties of the Steels

Figure 6 depicts the hardness, impact toughness, and bending strength of the four tested steels. It is evident that the changes in hardness are minimal with increasing preparation pressures; all samples exhibit similar hardness values exceeding HRC 60. Previous microstructure analysis indicates that under the four processing conditions, the microstructure of the prepared steel is composed of martensite and bainite. The microstructural and carbide distribution differences are negligible, which accounts for the minimal variation in hardness. For impact toughness, however, the values exhibit a nonlinear relationship with increasing pressure, and the toughness reaches a significant value of 3.95 J at 120 MPa, representing a 9% increase compared to the sample prepared at 0 MPa. This can be elucidated from various perspectives. On one side, the pressure applied during the squeeze casting process contributes to refining the grain structure of the alloy steels. The fine grain size significantly impedes crack propagation, thereby enhancing the toughness of the material. On the other side, defects such as porosity and inclusions during the casting process are mitigated to some extent when pressure is applied. These defects commonly serve as stress concentration points, thus reducing the toughness of the steel. Moreover, the application of pressure facilitates the uniform distribution of alloying elements and enhances the morphology and quantity of phases such as martensite and bainite, as mentioned above, thereby improving the overall mechanical properties of the material. This finding is also consistent with Khodaverdizadeh's study on the influence of exerted pressure on the mechanical characteristics of ductile iron prepared by the squeeze casting process [23].

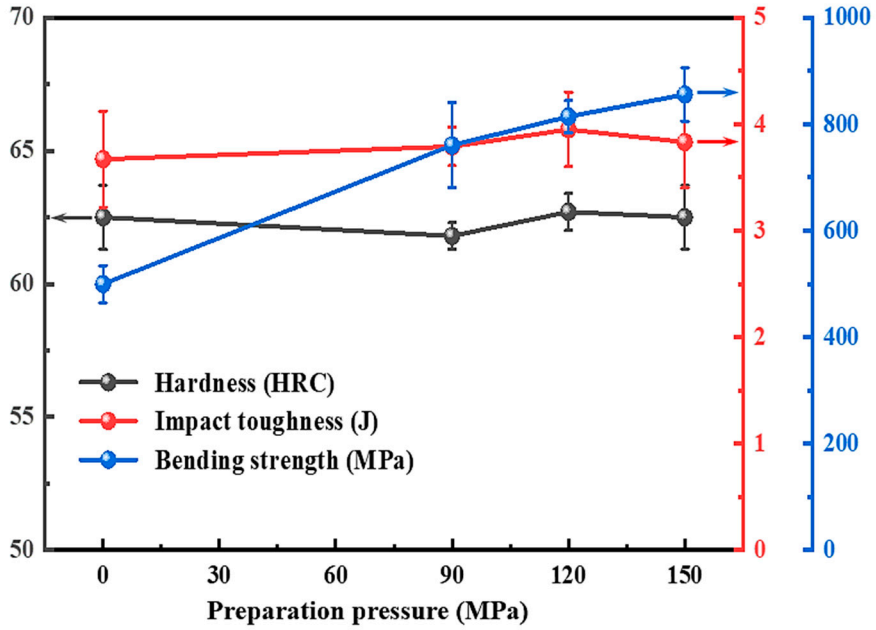

Figure 6. Mechanical properties including hardness, impact toughness, and bending strength of the samples prepared at various pressures.

Additionally, three-point bending strength exhibits a gradual increase with rising pressure, reaching a maximum value of 855.5 MPa when prepared under 150 MPa. According to the Hall–Petch equation, strength is inversely proportional to the square root of the grain diameter [20]: $\sigma = \sigma_0 + K/d^{1/2}$, where σ, σ_0, and d represent yield strength, intra-crystalline deformation resistance, and grain diameter, respectively. Consequently, finer grain sizes correlate with increased strength, and previous observations of the microstructures at varying pressures indicate that grain size progressively decreases with increasing pressure. Thus, the observed experimental changes in strength are justifiable. In terms of overall performance, the sample subjected to 120 MPa demonstrates superior

properties, and its relatively high hardness, impact toughness, and strength contribute to its optimal wear resistance (as described below).

Figure 7 illustrates the SEM micrograph of the fractured surface for the steels produced at 0 MPa and 120 MPa, respectively. As can be seen from the pictures, the fracture morphology of the sample fabricated without pressure illustrates distinct cleavage steps, a river pattern, and tongue-shaped pattern features, indicating that the fracture mechanism is characterized by a brittle destructive fracture. In contrast, the fracture of the sample prepared under pressure displays small dimples, along with cleavage steps and a tear ridge. The fracture mechanism is classified as a quasi-destructive fracture, resulting in superior toughness compared to the samples without exerted pressure.

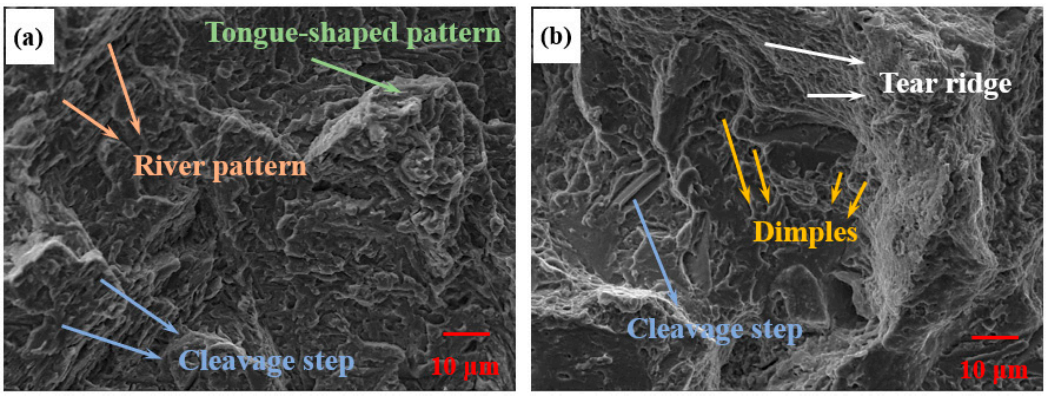

Figure 7. Fracture morphology of the prepared samples: (**a**) prepared under 0 MPa; (**b**) prepared under 120 MPa.

3.3. Impact–Abrasive Wear Performance and Worn Morphology

3.3.1. Wear Resistance Comparison

Impact–abrasive wear experiments were performed on the steels produced under four pressures (0, 90, 120, 150 MPa) at an impact energy of 3 J. Figure 8a exhibits the effect of the test duration on the worn weight loss of the four tested steels, with the loss recorded at 10 min intervals. For a specific energy, the wear volume loss exhibits an approximately linear increase with wear duration for the four steels. Analysis of the curves indicates that the increasing trend of steel manufactured without exerted pressure is much higher than that of the materials under pressure, and throughout the whole testing process, the former illustrated the highest cumulative weight loss, whereas the material under 120 MPa demonstrated the lowest values. The liner fit to the wear curves of the steels prepared under 0 MPa and 120 MPa were conducted as $y = 0.05615 + 0.01823x$ and $y = 0.01201 + 0.01314x$, respectively, where y represents wear loss, and x represents wear time. And the two fitting equations were all fitted with a confidence level greater than 95%. In addition, the wear rates for the four tested materials are shown in Figure 8b, and the wear rate per unit area of the steel prepared without pressure (0 MPa) is the maximum with a value of 1.0647 g/(h·cm^2), and the steel prepared under 120 MPa exhibits the minimum wear rate of 0.7879 g/(h·cm^2). Moreover, the wear rate decreased by 23.8% when the prepared pressure changed from 90 to 120 MPa, whereas the wear rate instead increased by 7.2% to 0.8445 g/(h·cm^2) when the applied pressure increased from 120 to 150 MPa.

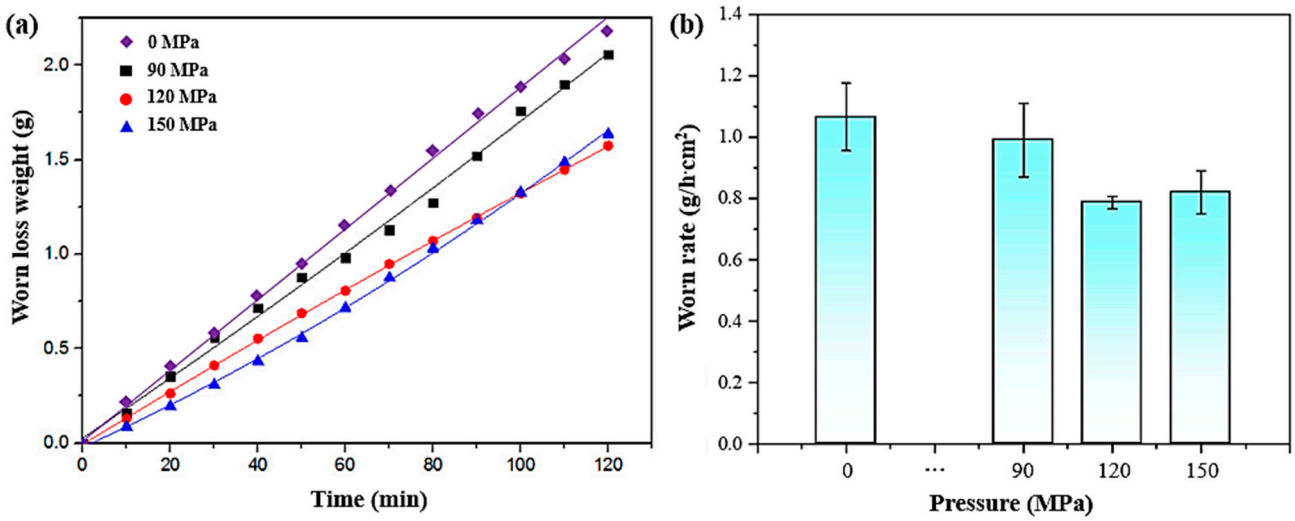

Figure 8. (**a**) Relationship between the worn time and wear weight loss of the steels produced at various pressures; (**b**) Average worn rate of the steels fabricated at various pressures.

3.3.2. Worn Surface Observation

For the purpose of obtaining a better understanding of the wear mechanism of the prepared Cr-Mn-Mo alloyed steel, the worn surfaces of the four tested steels under an energy of 3 J were investigated, and the results are shown in Figure 9. It is obvious that the steel prepared without pressure experienced more serious impact wear, which is evidenced by the rough worn surface, with some SiO_2 abrasive adhered to the worn surface and even embedded in it (Figure 9a,a′). Under the action of the impact hammer, the stress at the contact point of the abrasive and worn surface is high to facilitate cold welding, resulting in the bonding of the abrasive to the surface. Subsequently, the points of adhesion are sheared off during relative motion, resulting in the abrasive adhering to the worn surface [24]. In addition, the steel prepared without pressure lacks sufficient strength due to its larger grains, and abrasive particles are prone to embed in its worn surface. Furthermore, the curly abrasive debris and grooves with various size and shapes and the abrasive left on the surface after rolling and smoothing, as well as the pits, remained in certain regions due to the lack of the sufficient strength and fracture of the surface [25]. The findings indicate that the wear mechanism of the sample exhibits a combination of abrasive wear and adhesive wear.

Figure 9b,b′ illustrates the worn morphology of the steel prepared under 90 MPa, where wear characteristics such as grooves, cutting, and wear pits are evident. The grooves and cutting result from the abrasive properties of quartz sand, compounded by a wear process stemming from abrasive contact with a hard surface [26]. Consequently, softer surfaces experience repetitive loading, leading to deformation and fracture caused by the wear inflicted by small particles [27]. The cutting traces at high magnification are shown in Figure 9b′, where it can be seen that the bottom of the trace is uneven, featuring white, protruding ridge-like materials. The corresponding EDS analysis presented in Figure 10 indicates that these white ridge-like materials have a higher concentration of Fe and C. Based on the compositional design of the current alloy steel and the corresponding XRD patterns, it can be inferred that these white substances likely contain M_3C and M_7C_3 carbides. Consequently, the analysis of the wear mechanism of the steel under 90 MPa indicates that the relatively softer martensite and bainite matrix undergo initial wear, resulting in abrasive wear marks such as grooves. The hardness of the embedded M_3C and M_7C_3 carbides, which exceeds HV1200, enables their continued involvement in the wear process [28]. Moreover, these wear ridges, being embedded within the tougher martensite and bainite matrix, do not easily dislodge, thereby significantly enhancing wear performance.

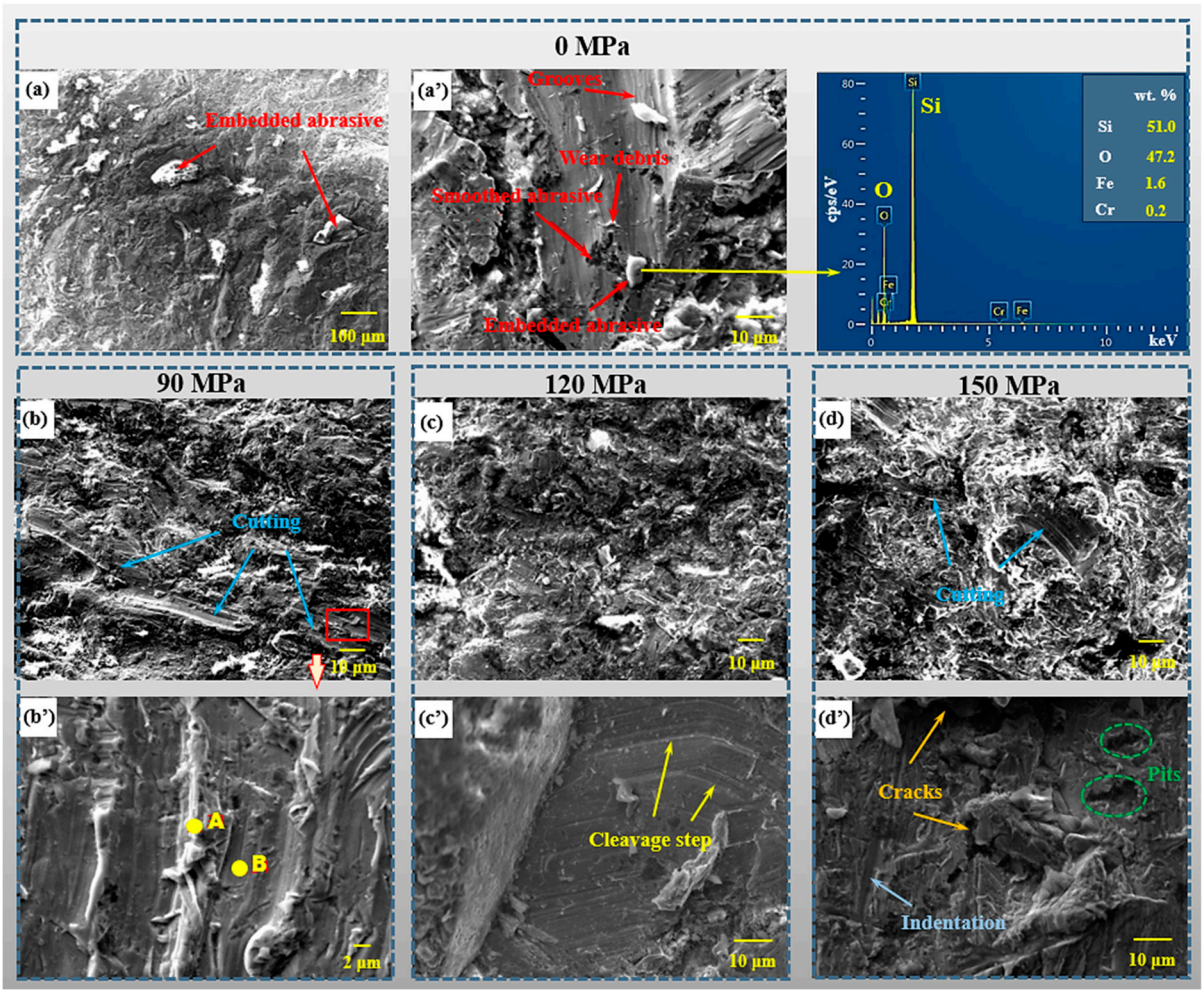

Figure 9. The worn morphology of the steels prepared under various pressures: (**a**,**a′**) 0 MPa; (**b**,**b′**) 90 MPa; (**c**,**c′**) 120 MPa; (**d**,**d′**) 150 MPa.

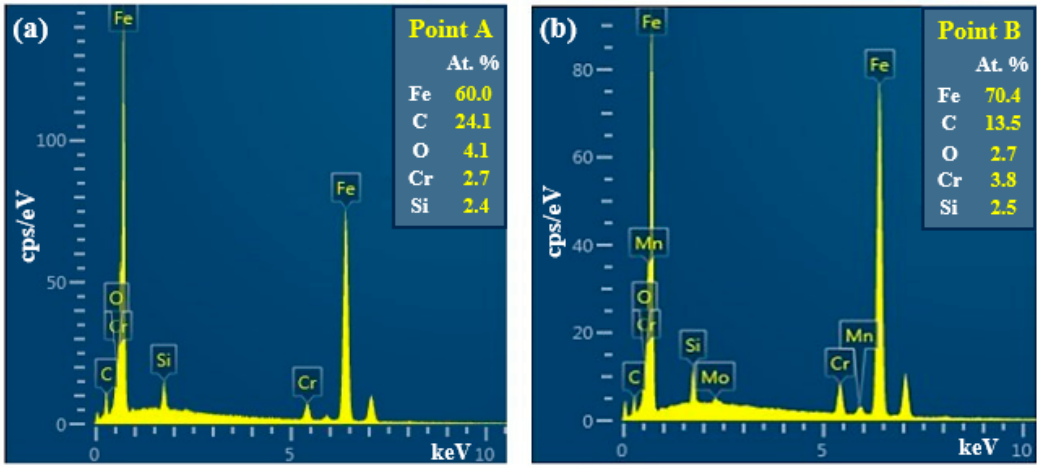

Figure 10. EDS results of Point A (**a**) and Point B (**b**) in Figure 9b′.

The worn surface of the steel prepared under 120 MPa after the wear test is shown in Figure 9c,c′. It can be seen that abrasive wear dominates the wear process, and the surface is covered with a mixture of displaced and deposited abrasive particles, along with quartz sand. Moreover, flaking pits are discernible on the worn surface, and their high-magnification diagram is presented in Figure 9c′, where a disintegration-step pattern is

evident, indicating that material spalling occurred through a brittle disintegration fracture mechanism. Figure 9d,d′ depicts the worn surface of the steel under 150 MPa, which consists of features such as grooves, cutting, wear debris, flaking pits, and accumulating ridges, implying that abrasive wear still plays a dominant role in the wear process. In addition, attributed to the impact cycle of the hammer, the fatigue source is produced due to the interaction between the sample and abrasive quartz sand. Once a crack initiates, subsequent impacts and deformations contribute to the extension and propagation of the crack, eventually connecting with adjacent cracks. The crack subsequently propagates in a direction parallel to the surface, with its depth being influenced by the material properties and the loading conditions. Upon reaching the surface, the crack shears and exfoliates into an elongated, thin wear flake, with its thickness being dependent on the position of the subsurface crack growth. Consequently, the presence of surface fatigue wear and abrasive wear leads to an intensification of the wear process; and the spalling pit facilitates the expansion of cracks, while the cracks diminish the strength of the matrix and enhance the cutting process, thus leading to an increased wear rate [29,30].

3.3.3. Wear Mechanism of the Samples

Figure 11 illustrates a schematic representation describing the impact–abrasive wear mechanism of the steels. During the wear process, the abrasive particles underwent repetitive sliding, pressing, and rolling on the wear surface [31]. For the sample prepared without pressure, given the lower hardness, the surface can easily generate larger grooves and cutting due to the sliding of sharp-angled abrasives. Given that the type of wear is associated with the contact angle formed by abrasive particles upon interaction with the wear surface, when the particle's angle of attack is significant, it results in cutting; in contrast, a smaller attack angle leads to the development of furrows. Furthermore, the material loss from cutting is typically more substantial than that resulting from furrowing (Figure 11a) [32]. Moreover, plastic deformation is also observed on the worn surface. When the abrasive particles collide with the surface at a high velocity, a high-energy impact is generated, causing plastic deformation in localized areas of the surface. Meanwhile, impact wear is a repetitive process, and after several impacts, the material gradually accumulates strain, leading to changes in the internal structure and also permanent plastic deformation [33]. In addition, under repeated impacts, the surface material experiences a plastic flow that can form localized ridges. As the material is crushed and deformed during wear, some of it may be pushed into neighboring areas, resulting in the formation of ridges (Figure 11b).

Furthermore, the spalling pits resulting from impact represent another characteristic associated with impact energy. As illustrated in Figure 11c, when the abrasive particles contact the sample, the wear surface experiences high-speed impacts from the abrasive, leading to the generation of impact pits. In addition, abrasive particles impact the material surface at a high velocity and frequency, causing localized stress concentrations. Cracking takes place when the stress surpasses the material's fatigue limit [34]. The inserted abrasive particle is another significant cause of material failure, as illustrated in the schematic in Figure 11d. The process can be outlined in several steps: first, brittle abrasive particles fracture upon the high-impact effect producing abrasive debris; next, sharp debris are pressed into the material, piercing it during the sliding action of the counterpart ring; subsequently, the cracks caused by penetration extend until they exceed the material's tensile strength; and finally, the material that penetrated the debris detaches from the surface and the mixture of the fragments and abrasive particles, resulting in further wear [35].

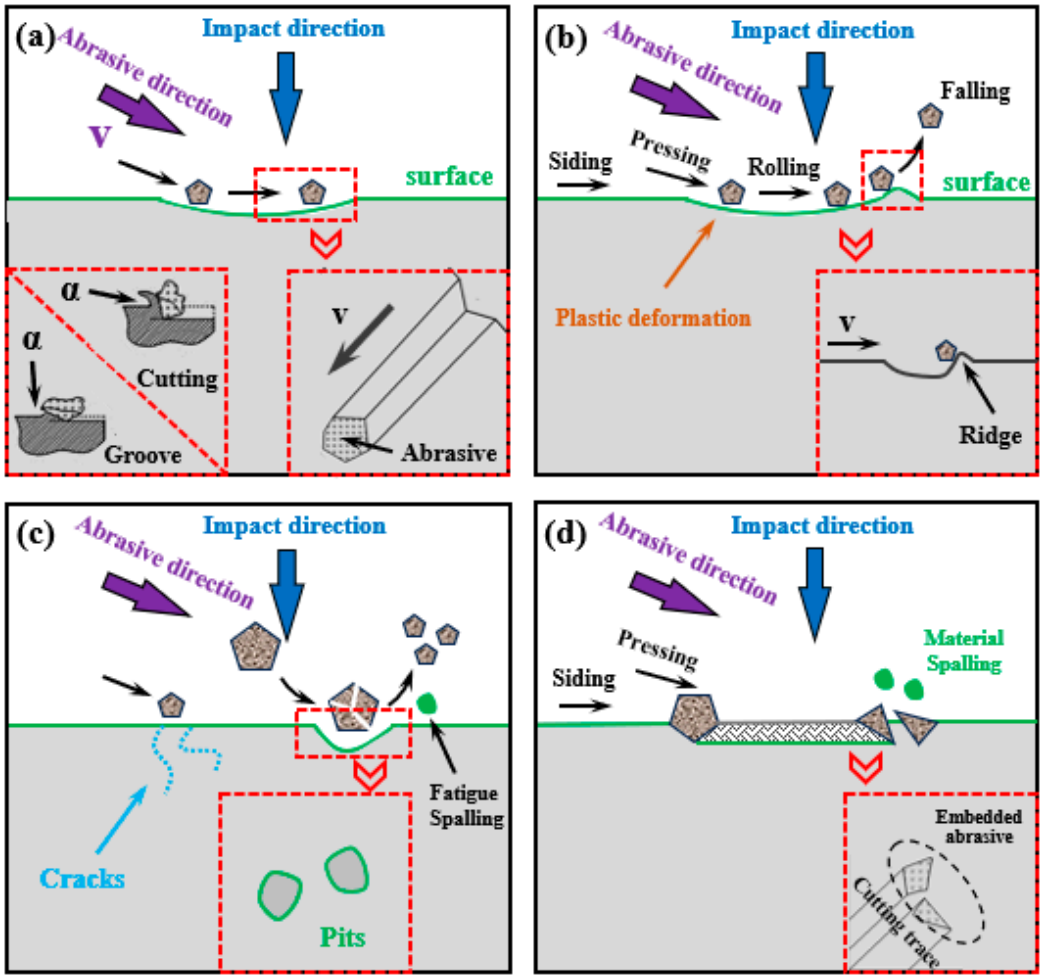

Figure 11. Schematic illustration of the wear mechanisms of the samples: (**a**) the formation of cutting and grooves; (**b**) the formation of ridges; (**c**) the formation of spalling pits; (**d**) the formation of inserted abrasive particles.

4. Conclusions

The squeeze casting process was employed to fabricate Cr-Mn-Mo alloyed steel liners. The effect of pressure on the microstructure, mechanical characteristics, and impact–abrasive wear resistance of the prepared steels was studied.

(1) The steels fabricated under pressure displayed smaller grains in comparison to those fabricated without pressure, which displayed thicker and longer primary dendrites. When contrasted with the unpressurized material, the grain diameter of the sample produced at 120 MPa decreased by 37.7%, the length of the primary arm shortened by 40.7%, and the spacing of the secondary arm contracted by 14.1%.

(2) The changes in hardness are minimal with increasing preparation pressures, and the tested samples exhibited similar hardness values exceeding HRC 60, which can be attributed to the comparable microstructure. The impact toughness results indicated that the samples prepared without pressure exhibited the characteristics of a brittle fracture, whereas a quasi-destructive fracture predominated in the samples prepared at 120 MPa. Additionally, the three-point bending strength exhibited a gradual increase with increasing pressure, reaching a maximum value of 855.5 MPa when prepared under 150 MPa.

(3) The impact–abrasive wear resistance of the Cr-Mn-Mo alloyed steel produced via squeeze casting was significantly enhanced compared to the samples produced without pressure. The samples without external pressure exhibited a combination of

abrasive and adhesive wear, whereas the wear characteristics of the samples prepared under pressure included grooves, cutting marks, flaking pits, and accumulating ridges. The slat martensite and bainite matrix, exhibiting superior toughness, supports the increased hardness of M3C and $M_{23}C_6$ carbides, which function as wear ridges during the wear process.

Author Contributions: Conceptualization, Y.Z.; methodology, Y.Z. and Y.H.; formal analysis, L.G. and X.W.; investigation, L.G. and X.W.; data curation, L.G. and X.W.; writing—original draft preparation, Y.Z. and Y.H.; writing—review and editing, L.G. and X.W.; project administration, Y.Z. All authors have read and agreed to the published version of the manuscript.

Funding: This research received no external funding.

Data Availability Statement: The data that support the findings of this study are available from the corresponding author upon reasonable request.

Conflicts of Interest: The authors declare no conflicts of interest.

References

1. Krbata, M.; Ciger, R.; Kohutiar, M.; Sozańska, M.; Eckert, M.; Barenyi, I.; Kianicova, M.; Jus, M.; Beronská, N.; Mendala, B.; et al. Effect of Supercritical Bending on the Mechanical & Tribological Properties of Inconel 625 Welded Using the Cold Metal Transfer Method on a 16Mo3 Steel Pipe. *Materials* **2023**, *16*, 5014. [CrossRef] [PubMed]
2. Krbata, M.; Eckert, M.; Majerik, J.; Barenyi, I. Wear Behaviour of High Strength Tool Steel 90MnCrV8 in Contact with Si3N4. *Metals* **2020**, *10*, 756. [CrossRef]
3. Li, J.; Xu, L.J.; Feng, Y.; Wu, S.B.; Li, W.; Wang, Q.W.; Zhang, P.; Tu, X.H. Hardening mechanism of high manganese steel during impact abrasive wear. *Eng. Fail. Anal.* **2023**, *154*, 107716. [CrossRef]
4. Shan, Q.; Ge, R.; Li, Z.; Zhou, Z.; Jiang, Y.; Lee, Y.S.; Wu, H. Wear properties of high-manganese steel strengthened with nano-sized V_2C precipitates. *Wear* **2021**, *482*, 203922. [CrossRef]
5. Zhang, J.H.; Patel, S.; Liu, Z.Y.; Lyu, T.; Wang, Y.H.; Hua, Y.J.; Simpers, J.H.; Vlasea, M. A data-driven framework to improve the wear resistance of a low-alloy steel fabricated by laser powder bed fusion. *J. Manuf. Process.* **2024**, *115*, 56–67. [CrossRef]
6. Wang, S.H.; Zhang, C.S.; Liu, J.M.; Li, H.; Zhao, D.G.; Ni, G.L. Effect of Solution Treatment on Microstructures and Mechanical Properties of High Nitrogen Stainless Steel. *Rare Met. Mater. Eng.* **2022**, *51*, 2761–2768.
7. Li, Z.L.; Jiang, Y.H.; Zhou, R.; Lu, D.H.; Zhou, R.F. Structural-Phase Composition and Hardness of Steel of the Fe-Cr-Mn-Mo-Al-Mg-N-C System Obtained by the Method of Self-Propagating High-Temperature Synthesis Under Nitrogen Pressure. *Metallurgist* **2023**, *67*, 1029–1037.
8. Li, S.S.; Zang, X.M.; Kong, L.Z.; Yang, J.; Jing, Y.A.; Wang, G.C. Suppressing interfacial reactions and burn-on defects in sand casted 13Cr9Mo1VNb steel castings. Part I: A novel MgO-chromite hybrid material. *Ceram. Int.* **2024**, *50*, 27835–27845. [CrossRef]
9. Patel, D.S.; Nayak, R.K. Blast Furnace Slag as an Alternative to Silica Sand for A356 Alloy Casting-Feasibility Study. *Int. J. Met.* **2024**, *18*, 2703–2720. [CrossRef]
10. Stan, I.; Anca, D.E.; Riposan, I.; Stan, S. Solidification pattern of 4.5%Si ductile iron in metal mould versus sand mould castings. *J. Therm. Anal. Calorim.* **2023**, *148*, 1805–1817. [CrossRef]
11. Pragathi, P.; Elansezhian, R. Mechanical and microstructure behaviour of aluminum nanocomposite fabricated by squeeze casting and ultrasonic aided squeeze casting: A comparative study. *J. Alloys Compd.* **2023**, *956*, 170203. [CrossRef]
12. Mourad, A.I.; Christy, J.V.; Krishnan, P.K.; Mozumder, M.S. Production of novel recycled hybrid metal matrix composites using optimized stir squeeze casting technique. *J. Manuf. Process.* **2023**, *88*, 45–58. [CrossRef]
13. Edosa, O.O.; Tekweme, F.K.; Gupta, K. Squeeze casting for metal alloys and composites: An overview of influence of process parameters on mechanical properties and microstructure. *China Foundry* **2023**, *20*, 148–158. [CrossRef]
14. Pennington, J.N. Squeeze-cast parts approach performance of forgings. *Mod. Met.* **1988**, *44*, 52–60.
15. Ganguly, S.; Reddy, S.T.; Majhi, J.; Nasker, P.; Mondal, A.K. Enhancing mechanical properties of squeeze-cast AZ91 magnesium alloy by combined additions of Sb and SiC nanoparticles. *Mater. Sci. Eng. A* **2021**, *799*, 140341. [CrossRef]
16. Murugadoss, P.; Jeyaseelan, C. Enhancing Tribo-Mechanical and Corrosion Properties of ADC 12 Alloy Composites through Marble Dust Reinforcement by Squeeze Casting Technique. *Materials* **2023**, *16*, 6374. [CrossRef]
17. Tirth, V.; Arabi, A. Effect of liquid forging pressure on solubility and freezing coefficients of cast aluminum 2124, 2218 and 6063 alloys. *Arch. Metall. Mater.* **2020**, *65*, 357–366. [CrossRef]
18. Nasker, P.; Mondal, A.K. SiC nanoparticles additions to squeeze-cast Mg-5.0Al-2.0Ca-0.3Mn alloy: An evaluation of microstructure and mechanical properties. *Mater. Charact.* **2024**, *212*, 113984. [CrossRef]
19. Tsai, Y.C.; Lee, S.L.; Lin, C.K. Effect of trace Ce addition on the microstructures and mechanical properties of A356(Al-7Si-0.35Mg) aluminum alloys. *J. Chin. Inst. Eng.* **2011**, *34*, 609–616. [CrossRef]
20. Zambrano, O.A. A Review on the effect of impact toughness and fracture toughness on impact-abrasion Wear. *J. Mater. Eng. Perform.* **2021**, *30*, 7101–7116. [CrossRef]

21. Qiu, B.; Xing, S.M.; Dong, Q.; Liu, H. Comparison of properties and impact abrasive wear performance of ZrO_2-Al_2O_3/Fe composite prepared by pressure casting and infiltration casting process. *Tribol. Int.* **2020**, *142*, 105979. [CrossRef]
22. Huang, Z.; Xing, J.; Gao, Y.; Cheng, X. Microstructure and properties of hypereutectic high chromium white cast iron prepared under pressure. *Ironmak. Steelmak.* **2011**, *38*, 359–362. [CrossRef]
23. Khodaverdizadeh, H.; Niroumand, B. Effects of applied pressure on microstructure and mechanical properties of squeeze cast ductile iron. *Mater. Des.* **2011**, *32*, 4747–4755. [CrossRef]
24. Zheng, J.; Li, W.; Li, J. A Comparative Study on the Wear Behavior of Quenched-and-Partitioned Steel (Q&P) and Martensite Steel (Q&T). *Coatings* **2024**, *14*, 727. [CrossRef]
25. Saha, G.; Valtonen, K.; Saastamoinen, A.; Peura, P.; Kuokkala, V.T. Impact-abrasive and abrasive wear behavior of low carbon steels with a range of hardness-toughness properties. *Wear* **2020**, *450*, 203263. [CrossRef]
26. Kohutiar, M.; Krbata, M.; Escherova, J.; Eckert, M.; Mikus, P.; Jus, M.; Polášek, M.; Janík, R.; Dubec, A. The Influence of the Geometry of Movement during the Friction Process on the Change in the Tribological Properties of 30CrNiMo8 Steel in Contact with a G40 Steel Ball. *Materials* **2024**, *17*, 127. [CrossRef]
27. Lu, D.S.; Liu, Z.Y.; Li, W.; Liao, Z.; Tian, H.; Xian, J.Z. Influence of carbon content on wear resistance and wear mechanism of Mn13Cr2 and Mn18Cr2 cast steels. *China Foundry* **2015**, *12*, 39–47.
28. Wang, C.Y.; Li, X.D.; Chang, Y.; Han, S.; Dong, H. Comparison of three-body impact abrasive wear behaviors for quenching-partitioning-tempering and quenching-tempering 20Si2Ni3 steels. *Wear* **2016**, *362*, 121–128. [CrossRef]
29. Wang, X.D.; Chen, Y.B.; Wei, S.Z.; Zuo, L.L.; Mao, F. Effect of Carbon Content on Abrasive Impact Wear Behavior of Cr-Si-Mn Low Alloy Wear Resistant Cast Steels. *Front. Mater.* **2019**, *6*, 153. [CrossRef]
30. Lu, J.; Yu, H.; Kang, P.F.; Duan, X.N.; Song, C.H. Study of microstructure, mechanical properties and impact-abrasive wear behavior of medium-carbon steel treated by quenching and partitioning (Q&P) process. *Wear* **2018**, *414*, 21–30.
31. Fu, H.; Chen, P.; Huang, X.D.; Zhang, W.G.; Wang, R.; Huang, Q.Y.; Shan, Q. Effect of N and aging treatment on precipitation behavior, mechanical properties and wear resistance of Ti–V–Nb alloyed high manganese steel. *J. Mater. Res. Technol.* **2024**, *29*, 1949–1961. [CrossRef]
32. Qiu, B.; Xing, S.M.; Dong, Q. Fabrication and wear behavior of ZTA particles reinforced iron matrix composite produced by flow mixing and pressure compositing. *Wear* **2019**, *428*, 167–177. [CrossRef]
33. Deng, X.T.; Wang, Z.D.; Han, Y.; Zhao, H.; Wang, G.D. Microstructure and Abrasive Wear Behavior of Medium Carbon Low Alloy Martensitic Abrasion Resistant Steel. *J. Iron Steel Res. Int.* **2014**, *21*, 98–103. [CrossRef]
34. Song, K.L.; Yang, S.S.; Xie, L.P.; Chen, M.H.; Wang, F.H. Mechanical and Wear Behavior of Cobalt Based Composite with In-Situ Carbide Formed via Decomposition of Ti_3SiC_2. *Metall. Mater. Trans. A* **2024**, *55*, 1495–1508. [CrossRef]
35. Wang, W.; Song, R.B.; Peng, S.G.; Pei, Z.Z. Multiphase steel with improved impact-abrasive wear resistance in comparison with conventional Hadfield steel. *Mater. Des.* **2016**, *105*, 96–105. [CrossRef]